Interfacial engineering of CoMn$_2$O$_4$/NC induced electronic delocalization boosts electrocatalytic nitrogen oxyanions reduction to ammonia

Zhaodong Niu [a], Shiying Fan [a], Xinyong Li [a,*], Jun Duan [a], Aicheng Chen [b]

[a] State Key Laboratory of Fine Chemicals and Key Laboratory of Industrial Ecology and Environmental Engineering, School of Environmental Science & Technology, Dalian University of Technology, Dalian 116024, China
[b] Electrochemical Technology Center, Department of Chemistry, University of Guelph, 50 Stone Road East, Guelph, ON N1G 2W1, Canada

ARTICLE INFO

ABSTRACT

Electrocatalytic nitrate (NO$_3^-$) reduction reaction (NO$_3$RR) is a promising avenue for wastewater treatment and value-added ammonia (NH$_3$) generation. Herein, cobalt manganese spinel nanoparticles embedded in multi-channel carbon fibers (CoMn$_2$O$_4$/NC) to obtain optimal NH$_3$ Faradaic efficiency is 92.4% with a yield rate of 144.5 mmol h^{-1} g^{-1} at $-$ 0.7 V versus reversible hydrogen electrode (vs. RHE). The interfacial between CoMn$_2$O$_4$ and NC induces the 3d orbital electrons of Co and Mn in less localized states, which promotes *NH$_3$ desorption. Electrochemical in situ Raman spectra and online differential electrochemical mass spectrometry (DEMS) identified the intermediates and products. The theoretical calculation demonstrates that the existence of NC could reduce the free energy difference of the rate-determining step (RDS, 0.42 eV) of NO$_3$RR, suppressing hydrogen evolution reaction (HER) by enhancing the interaction of *H. Coupled benzyl alcohol oxidation reaction (BOR) with NO$_2^-$RR to obtain lower reduction voltage and high value-added anode products.

1. Introduction

Ammonia (NH$_3$) is an essential feedstock in the manufacture of fertilizer, chemical industry and medicine industries [1]. It has been considered one of the most competitive candidates for next-generation energy carrier molecules due to its high hydrogen content (17.65%). The NH$_3$ synthesis industry mainly relies on the energy-intensive Haber-Bosch process (HBP). Although, the novel electrocatalytic nitrogen reduction reaction (NRR) powered by renewable energy has received much attention as an alternative [2–4]. Yet, the ultrahigh triple bond dissociation energy of N$_2$ molecules (~941 kJ mol^{-1}) endows the inherent sluggish kinetics [5,6]. To our knowledge, nitrate (NO$_3^-$) is a primary nitrogen cycle carrier with appropriate N═O splitting energy (204 kJ mol^{-1}) [7,8]. It mainly originates from agricultural runoff and industrial wastewater, which induces eutrophication of water bodies and threatens human health [9,10]. In addition, the recent plasma nitrogen oxidation technology converts air to NO$_3^-$ at a low cost [11]. The electrocatalytic nitrate reduction (NO$_3^-$RR) is an amazingly sustainable route for producing "green" NH$_3$ and can simultaneously reduce its pollution of the environment [12–14]. In which water molecules as the proton source and conducted under ambient conditions. Although noble metals (Pd, Ru and Ag) [15–17], non-precious metals (Cu, Ti, Co and

Mn) [18–21], and their composite material are widely reported for NH$_3$ production from NO$_3^-$RR [22,23], obtaining high catalytic activity remains a challenge.

The electrochemical NO$_3^-$RR to produce NH$_3$ involves multiple electrons and protons transfer, i.e., eight-electron and nine proton processes under a neutral medium. There are inevitably many intermediate species, and nitrite (NO$_2^-$) is the most famous by-product of desorption the *NO$_2$ [24,25]. On the other hand, the competitive hydrogen evolution reaction (HER) is also one of the important factors restricting the electrochemical synthesis of NH$_3$ in neutral electrolytes [26,27], especially under high current densities. Interface engineering can optimize the adsorption behavior of key intermediate species on the active sites of the catalyst surface and optimize the reaction pathway to promote electrochemical NO$_3^-$RR into NH$_3$ [21,28]. More recently, He et al. reported a novel NO$_3^-$ tandem electrocatalytic strategy for high-rate NH$_3$ production, of which Cu/CuO$_x$ and Co/CoO phases serve NO$_3^-$-to-NO$_2^-$ and NO$_2^-$-to-NH$_3$, respectively [29]. Porous carbon has been widely used in various electrochemical studies as an inexpensive and efficient electrocatalytic material [30,31]. For instance, the efficient electronic coupling effect between niobium titanium oxide (NbTiO$_4$) nanoparticles on nitrogen-doped carbon nanorods (NCNR) facilitates the electrocatalytic reduction of N$_2$ to NH$_3$ [32]. Although the porous carbon

matrix can adjust the surface electronic structure of metal oxide catalysts, its application in electrochemical NO_3^-RR is still lacking, especially the in-depth understanding of catalyst and surface electronic structure differences.

Herein, we reported cobalt manganese spinel nanoparticles supported on multichannel carbon fibers ($CoMn_2O_4$/NC) as electrocatalysts for NO_3^-RR to NH_3 at 0.1 M Na_2SO_4 solution. The $CoMn_2O_4$/NC had an outstanding electrochemical performance for NH_3 synthesis. The maximum NH_3 Faradaic efficiency of NO_3^-RR reached 92.4% at − 0.7 V versus reversible hydrogen electrode (vs. RHE) with a yield rate of 144.5 mmol h^{-1} g^{-1}. The 3d orbital of Co and Mn in $CoMn_2O_4$/NC are less localization induced by existing carbon species, which can promote the conversion of NO_3^--to-NH_3 by reducing the free energy difference (ΔG) of the rate-determining step (RDS, *0.42 eV*). Electrochemical in situ Raman spectra were employed to explore the stability of the catalysts and the possible intermediate species at the nitrogen oxyanions (i.e., NO_3^- and NO_2^-) reduction. Moreover, we present an effective strategy to enhance the energy efficiency by coupling BOR with NO_2^-RR by replacing the anode OER and obtaining low reduction voltage and high value-added anode products.

2. Experimental

2.1. Chemicals and materials

Polyacrylonitrile (PAN, Mw = 150,000), polystyrene (PS), manganese acetate (Mn(CH$_3$COO)$_2$·4 H$_2$O, 99%), cobalt acetate (Co (CH$_3$COO)$_2$·4 H$_2$O, 99.5%), N,N-Dimethylformamide (DMF, 99.5%), sodium nitroferric cyanide (C$_5$FeN$_6$Na$_2$O, 99%), salicylic acid (99.5%), sodium citrate dihydrate (99%), sodium hydroxide (NaOH, 96%), sodium hypochlorite (NaClO), sodium sulfate (Na$_2$SO$_4$, 99%), sodium nitrate (NaNO$_3$, 99%), sodium nitrate-^{15}N (Na^{15}NO$_3$, 98.5%) and maleic acid (MA, 99%) were used as received without further purification. Nafion (5 wt%) and proton-exchange membrane of 117 was obtained from Dupont. Carbon cloth (HCP330N) was supplied by Hesen Co., Ltd.

2.2. Synthesis of CoMn$_2$O$_4$/NC

The CoMn$_2$O$_4$/NC was prepared according to the previously reported method with some modifications [33]. 1 g of PAN and 0.8 g of PS were dispersed into 10 mL of DMF at 60 °C with magnetic stirring for 8 h to obtain a uniform solution. Then, 1 mmol of Mn(CH$_3$COO)$_2$·4 H$_2$O and 0.5 mmol of Co(CH$_3$COO)$_2$·4 H$_2$O were added to the above solution with vigorous stirring at room temperature overnight. The precursor solution was loaded into a plastic syringe with a stainless-steel needle. The aluminum (Al) foil was used as a collector of electrospun fibers, 15 cm away from the needle. The positive voltage of 17 kV was applied with a flow rate of 1 mL h^{-1}. The obtained precursor fibers were dried in a vacuum oven at 70 °C for 8 h. The precursor fibers were stabilized at 200 °C and maintained for 2 h with 2 °C min^{-1}. Then, the precursor fibers were placed in the tube furnace and carbonized at 800 °C for 2 h with a heating rate of 3 °C min^{-1} under N$_2$ flow to obtained CoMn$_2$O$_x$/NC. Finally, the CoMn$_2$O$_x$/NC was placed in a muffle furnace and calcined to 300 °C with a heating rate of 2 °C min^{-1} for 2 h in air flow to obtained CoMn$_2$O$_4$/NC. The CoMn$_2$O$_4$ was prepared by directly calcining CoMn$_2$O$_x$/NC at 500 °C in air for 2 h. The NC was synthesized by a similar method to CoMn$_2$O$_4$/NC without adding metal salt to the precursor solution.

2.3. Characterization

X-ray diffraction (XRD) patterns were carried out on Bruker D8 Advance with a Cu Kα radiation (λ = 0.15418 nm). Field-emission scanning transmission microscope (FESEM) conducted under JEOL (JSM-7900 F). High-resolution transmission electron microscope (HRTEM) was measured using JEOL (JEM F200) with an energy-

dispersive X-ray spectroscopy (EDX) detector. X-ray photoelectron spectroscopy (XPS) were carried out using an X-ray photoelectron spectrometer (Thermos K-Alpha +) with Al Kα as the X-ray source. N$_2$ adsorption-desorption isotherms were measured by Quanta chrome (NOVA 4200e) at 77 K. The NH$_3$ was confirmed using ^{1}H nuclear magnetic resonance (^{1}H NMR, Bruker 400 MHz) with 0.1 M Na^{15}NO$_3$ was employed as the nitrogen source.

2.4. Electrochemical measurements

All electrochemical measurements were performed on a CHI 660E electrochemical workstation (China Chenhua). The electrolytic cell was using a homemade two-compartment cell with a separate membrane of Nafion 117. The Ag/AgCl (saturated KCl solution) and Pt plate (1 × 1.5 cm^2) electrodes were used as the reference and counter electrode, respectively. For the working electrode prepared, firstly, 10 mg of catalyst was dispersed in a mixture of 720 μL of ethanol, 240 μL of water and 40 μL of Nafion (5 wt%) with sonication for 1 h to form a homogenous ink. Then, 40 μL of ink was dropped onto a piece of carbon cloth (1 × 1 cm^2) as a working electrode (0.4 mg cm^{-2}). All potentials were converted based on the Nernst equation of E$_{RHE}$ = E$_{Ag/AgCl}$ + 0.0591 × pH + 0.197 × V. Linear sweep voltammetry (LSV) curves were measured with a scan rate of 50 mV s^{-1}. The double-layer capacitance (C$_{dl}$) values were calculated based on cyclic voltammetry (CV) curves at a non-Faradaic region with a scan rate of 20 ∼ 100 mV s^{-1}. The electrochemical active surface area (ECSA) was calculated by the following equation:

$$\Delta J = (J_a - J_c)/2$$

$$ECSA = C_{dl}/C_s$$

where J_a and J_c are the current densities of the anode and cathode, respectively. Then the C_{dl} value was obtained by plotting a function between the "ΔJ" and "scan rate". The average specific capacitance (C$_s$) of a flat unit plane electrode (1 cm^{-2}) is generally 40 μF cm^{-2}.

For two electrode configuration, nickel foam (1 × 1 cm^2) and CoMn$_2$O$_4$/NC loaded carbon cloth (1 × 1 cm^2, 0.4 mg cm^{-2}) were used as anode and cathode, respectively. The anode and cathode electrolytes consisted of 1 M KOH with 0.1 M benzyl alcohol (BA) and 0.1 M Na$_2$SO$_4$ with 0.1 M NO$_2^-$, respectively. All the curves were obtained without IR compensation and measured in Ar-saturated electrolyte.

2.5. Determination of products

NH$_3$ detection. The generated NH$_3$ was detected by the indophenol blue method. A certain amount of the electrolyte was taken from the cathode cell after reaction for 1 h and diluted with fresh electrolyte to 1 mL. Afterwards, 1 mL of 1 M NaOH solution containing 5 wt% salicylic acid and 5 wt% sodium citrate dihydrate was added. Then, 0.5 mL of 0.05 M NaClO and 0.1 mL of C$_5$FeN$_6$Na$_2$O (1 wt%) were added into the above solution. After standing at ambient conditions for 2 h, the ultraviolet-visible absorption was recorded at 654 nm. Besides, the ^{1}H NMR was employed to verify the indophenol blue method. After the reaction, the pH of the electrolyte was adjusted to weak acid with a 4 M H$_2$SO$_4$ solution. The maleic acid (MA) and deuterium oxide (D$_2$O) was used as the internal standard and deuterium reagent, respectively.

NO$_2^-$ detection. The concentration of NO$_2^-$ was analyzed with the Griess test. A certain amount of the electrolyte was taken from the cathode cell after reaction for 1 h and diluted with fresh electrolyte to 1 mL. Then, 2 mL of water and 1 mL of Griess reagent were added into 1 mL of diluted electrolyte. After standing at ambient conditions for 10 min, the ultraviolet-visible absorption was recorded at 540 nm. The Griess reagent was configured by dissolving of 4 g of sulfonamide, 0.2 g of N-(1-naphthyl)-ethylenediamine dihydrochloride and 10 mL of phosphoric acid in 50 deionized H$_2$O.

N₂H₄ detection. The produced hydrazine (N$_2$H$_4$) was detected by a chromogenic method (i.e., Watt and Christo). Typically, 0.599 g of p-dimethylaminobenzaldehyde (C$_9$H$_{11}$NO), 3 mL of concentrated hydrochloric acid (HCl) and 30 mL of ethanol were mixed to prepare the chromogenic reagent. Then, 1 mL of reagent was added into 1 mL of electrolyte. After standing at ambient conditions for 30 min, the ultraviolet-visible absorption was recorded at 458 nm.

H₂ detection. Quantitative analysis of the produced H$_2$ was measured by a gas chromatography (GC-7890A, Agilent) equipped with thermal conductivity detector (TCD).

The anode products (i.e., benzoic acid and benzaldehyde) were detected by the high-performance liquid chromatography (HPLC, Agilent, C18 column and 254 nm). The mobile phase is methanol-water (70:30) with a flow rate of 0.8 mL min^{-1}.

The Faradaic efficiency, yield rate and partial current density were calculated by the following equation:

Faradaic   efficiency $= (nF \times c \times V)/(M \times Q) \times 100\%$

Yield   rate $= (c \times V)/(M \times t \times m)$

Partial   current   density $= (FE \times Q)/t$

where n is the number of electrons transferred, F is the Faradaic constant (96,485 C mol^{-1}), c is the concentration of products, V is the volume of catholyte (0.04 L), M is the relative molecular mass, Q is the total charge (C), t is the electroreduction time (h) and m is the mass of the catalyst on the cathode (g).

2.6. Energy consumption efficiency

The relative energy consumption of NH$_3$ production from electrochemical NO$_2^-$RR in the two-electrode system is calculated as follows:

Energy   consumption   saving $= (U_2 - U_1)/U_2 \times 100\%$

where U_1 and U_2 are the voltages for a certain amount of NH$_3$ production from NO$_2^-$RR||OER and NO$_2^-$RR||BOR under different current densities, respectively.

2.7. In situ Raman measurement

In situ Raman spectroscopy was performed on a Renishaw inVia Qontor Raman microscope system with a homemade three-electrode H-type in situ cell. The wavelength of the excitation source of the laser is 532 nm (10%). A 50 × long focal length distance objective (Leica) was used for focus. The graphite rod and Ag/AgCl electrode (saturated KCl solution) as the counter and reference electrodes, respectively. The spectrum was collected after 5 min of stable operation for each potential.

2.8. In situ differential electrochemical mass spectrometry (DEMS) measurement

In situ DEMS measurements were used to detect intermediates and products of the NO$_3^-$RR process. Typically, 20 µL of catalyst ink (2 mg mL^{-1}) was applied dropwise on PTFE membrane to prepare a working electrode and conductively connected through gold (Au) foil. The platinum wire and Ag/AgCl electrode were adopted as counter and reference electrodes, respectively. Ar-saturated 0.1 M Na$_2$SO$_4$ containing 0.1 M NaNO$_3$ as an electrolyte. The voltage range during the test was − 0.5 to − 1.6 V at a scan rate of 6 mV s^{-1}. After the baseline was kept steady, the possible intermediate and product were collected during the electrocatalysis process. The test terminated after four cycles.

2.9. Theoretical calculations

Density functional theory (DFT) were carried out to calculate the conversion of NO$_3^-$ into NH$_3$ on CoMn$_2$O$_4$/NC and CoMn$_2$O$_4$ by using the Vienna ab initio simulation package (VASP) code [34,35]. The projector augmented wave (PAW) approach was adopted to describe the ion-electron interaction [36]. The generalized gradient approximation (GGA) in the form of the Perdew-Burke-Ernzerhof (PBE) functional was applied to describe the electron exchange and correlation energy [37]. The cut-off energy and energy convergence were set to 400 eV and 1×10^{-5} eV, respectively, to perform all computations. A Monkhorst-Pack k-point mesh of $4 \times 4 \times 1$ was used for CoMn$_2$O$_4$/NC and CoMn$_2$O$_4$ surface models. A vacuum space with 15 Å was inserted in the z-direction to prevent the artificial interaction between periodically repeated images. The chemical potential of a proton-electron pair ($\mu(H^+) + \mu(e^-)$) is equal to the half of the chemical potential of one gaseous hydrogen ($1/2 \, \mu(H_2)$). To avoid the influence of the negative charge, both NO$_3^-$ and NO$_2^-$ were replaced by nitric acid (HNO$_3$) and nitrous acid (HNO$_2$). The Gibbs free energies of the reaction were calculated as follows equation (U = 0 and pH = 7):

$$\Delta G = \Delta E + \Delta ZPE - T\Delta S$$

where ΔE is the reaction energy difference between the products and reactants; ΔZPE is the change of zero-point energy; ΔS and T (298 K) is entropy change and temperature, respectively.

3. Result and discussion

3.1. Morphological and structural characterizations

The preparation of highly dispersed CoMn$_2$O$_4$/NC is schematically illustrated in Fig. 1a. Typically, precursor fibers (i.e., PAN/PS/(CoMn$_2$)) were firstly fabricated by an electrospinning method. Then the composite fibers were pyrolysis (i.e., carbonization and oxidation) to fabricate multichannel carbon fibers with highly dispersed CoMn$_2$O$_4$ spinel nanoparticles. The scanning electron microscopy (SEM) and transmission electron microscopy (TEM) were conducted to reveal the morphology of the prepared materials. The SEM image indicated that the precursor fibers were continuous solid structures with a smooth surface (Fig. S1a). Notably, after pyrolysis, the morphology features of CoMn$_2$O$_4$/NC demonstrated hollow multichannel fibers with a rough surface (Fig. 1b). The NC exhibits similar structural properties, except for the smooth surface (Fig. S1b). By contrast, the structure of CoMn$_2$O$_4$ appears to collapse due to the removal of multichannel carbon fibers (Fig. S1c). It is worth noting that the CoMn$_2$O$_4$ nanoparticles no evidently agglomeration, indicating their high dispersibility. The above results were also evidenced by TEM and high-angle annular dark field scanning TEM (HAADF-STEM) images (Fig. 1c-e). As shown in Fig. 1c, the TEM image of CoMn$_2$O$_4$/NC indicate that the CoMn$_2$O$_4$ nanoparticles were dispersed and embedded in the NC. The HR-TEM image demonstrated that the lattice fringes with a spacing of about 0.25 nm attribute to the (211) planes of CoMn$_2$O$_4$ with the graphitized carbon surrounding (Fig. 1d). Furthermore, the elemental mapping images analysis revealed that C, N, O, Co and Mn elements were uniformly dispersed on CoMn$_2$O$_4$/NC (Fig. 1f-j).

The X-ray diffraction (XRD) pattern analysis demonstrated that CoMn$_2$O$_4$ shows a standard spinel structure (PDF#77–0471) (Fig. S2a) [38], and NC reveals two solitary diffraction peaks at about 25 and 44°, which belong to graphitic carbon (Fig. S2b) [39]. Notably, CoMn$_2$O$_4$/NC well integrated the characteristic peaks of CoMn$_2$O$_4$ and NC (Fig. 2a), consistent with the TEM results. X-ray photoelectron spectroscopy (XPS) was performed to investigate the intrinsic electronic structure of Co and Mn in CoMn$_2$O$_4$/NC and CoMn$_2$O$_4$ (Fig. S3). The high-resolution Co 2p spectra of CoMn$_2$O$_4$ were fitted with two main peaks at about 781.1 eV (2p$_{1/2}$) and 796.7 eV (2p$_{3/2}$), separated by about of 15.6 eV (Fig. S4a),
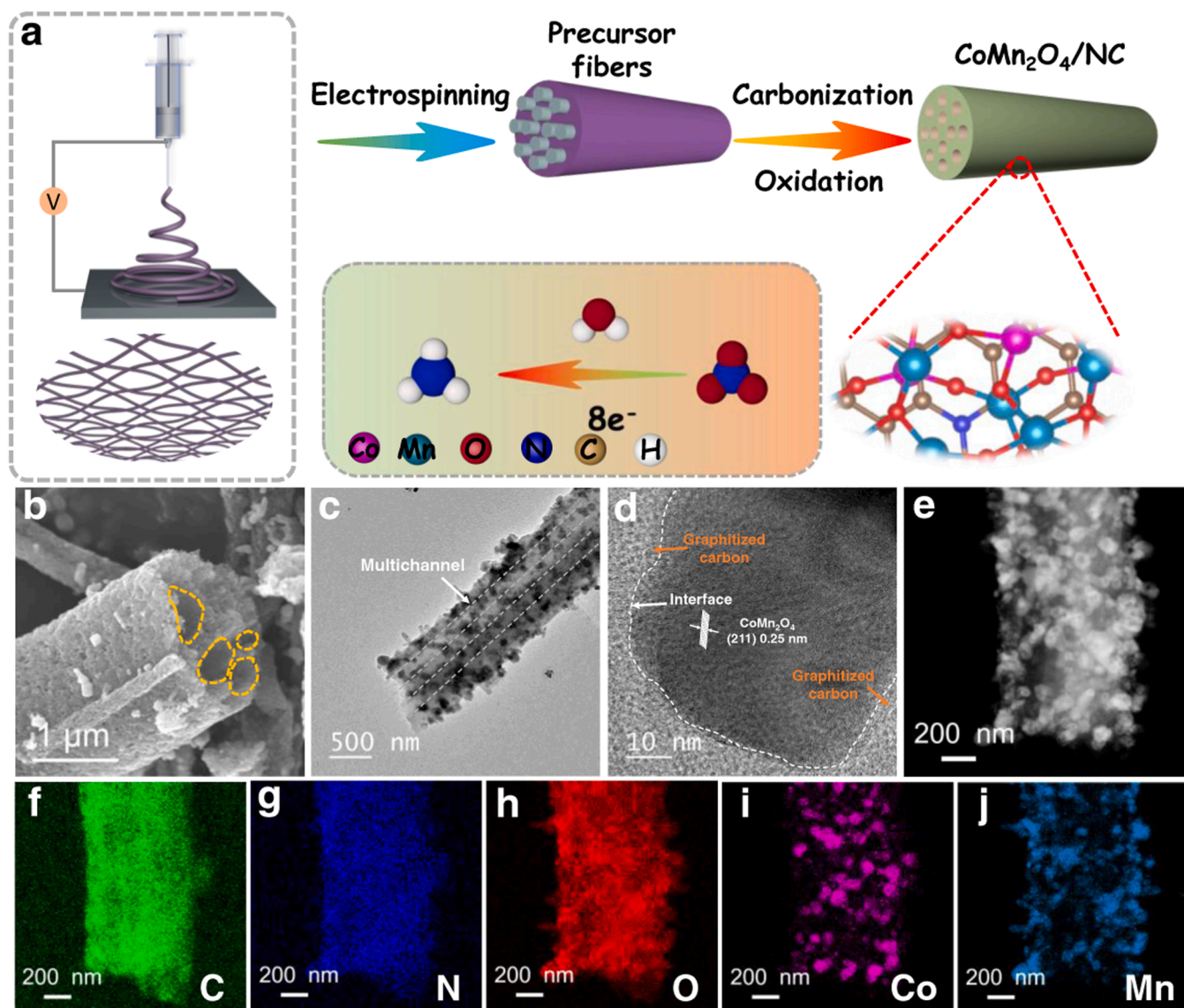
Fig. 1. (a) Illustration of the preparation of $CoMn_2O_4/NC$ for electroreduction NO_3^- to NH_3. (b) SEM, (c) TEM and (d) HR-TEM images of $CoMn_2O_4/NC$. (e) HAADF-STEM image and (f-j) the corresponding elemental mapping images of C, N, O, Co and Mn, respectively.

consistent with the Co^{2+} species [38]. Additionally, the distinct satellite peak at about 786.3 eV, indicating the Co element exists in the form of Co^{2+} species. Notably, the presence of carbon species (i.e., $CoMn_2O_4/NC$) shifts the Co 2p peak slightly towards higher binding energies (0.6 eV) (Fig. 2b), and the Co element still exists as Co^{2+}. The high-resolution Mn 2p spectra of $CoMn_2O_4/NC$ and $CoMn_2O_4$ display two peaks of spin-orbit splitting Mn species, corresponding to Mn $2p_{1/2}$ and Mn $2p_{3/2}$ (Fig. 2c and S4b) [40], respectively. The Mn $2p_{3/2}$ spectrum was deconvoluted to three peaks of Mn^{2+}, Mn^{3+} and Mn^{4+} at the binding energy of about 641, 642 and 644 eV [41], respectively. More importantly, the average valence states of Mn on $CoMn_2O_4$ and $CoMn_2O_4/NC$ are about 2.97 and 3.18, respectively (Table S1), implying the Mn mainly occupies octahedral sites. The N 1 s spectra confirmed that $CoMn_2O_4$ does not have carbon matrix residues (Fig. S5). The density of state (DOS) of Co 3d, Mn 3d and O 2p orbitals centers were also investigated to reveal the electronic structure of $CoMn_2O_4$ and $CoMn_2O_4/NC$ (Fig. 2d-f and S6). Compared with $CoMn_2O_4$, the 3d states of Co and Mn in $CoMn_2O_4/NC$ are less localized, especially for Co $3d_{xz}$ and Mn $3d_x^2$ orbitals. Furthermore, the O 2p orbitals of $CoMn_2O_4$ and $CoMn_2O_4/NC$ are less different, but the resonate interval of $CoMn_2O_4/NC$ is more positive. The above results confirm that the existence of carbon species

can significantly tailor the electronic structure of $CoMn_2O_4$, i.e., the electronic delocalization effect, which contributes to the desorption of $*NH_3$.

3.2. Electrocatalytic performance for NO_x^-RR

The electrochemical activity of $CoMn_2O_4/NC$ for NO_3^-RR was evaluated in a three-electrode electrolytic cell (gas tight H-type) separated by a proton exchange membrane. As shown in Fig. 3a, the linear sweep voltammetry (LSV) curves of NO_3^-RR display a more positive onset potential (1 mA cm^{-2}) for $CoMn_2O_4/NC$ (+0.2 V vs. RHE) than that of $CoMn_2O_4$ (−0.6 V vs. RHE) and NC (−0.8 V vs. RHE). As expected, $CoMn_2O_4/NC$ also exhibited the best current density response with decreasing potential, suggesting it has an excellent activity for NO_3^-RR. It is worth noting that the specific surface area of $CoMn_2O_4/NC$ is 400.6 cm^2 g^{-1}, which is 31.3 times that of $CoMn_2O_4$ (12.8 cm^2 g^{-1}) (Fig. S7), endowing $CoMn_2O_4/NC$ with an excellent electrochemically active area (Fig. S8). Notably, the response of the current density of $CoMn_2O_4/NC$ to NO_3^- concentration is positively correlated (Fig. S9a). The NH_3 Faradaic efficiency was increased gradually with the increase of NO_3^- concentration (Fig. S9b). The performance of NO_3^-RR was
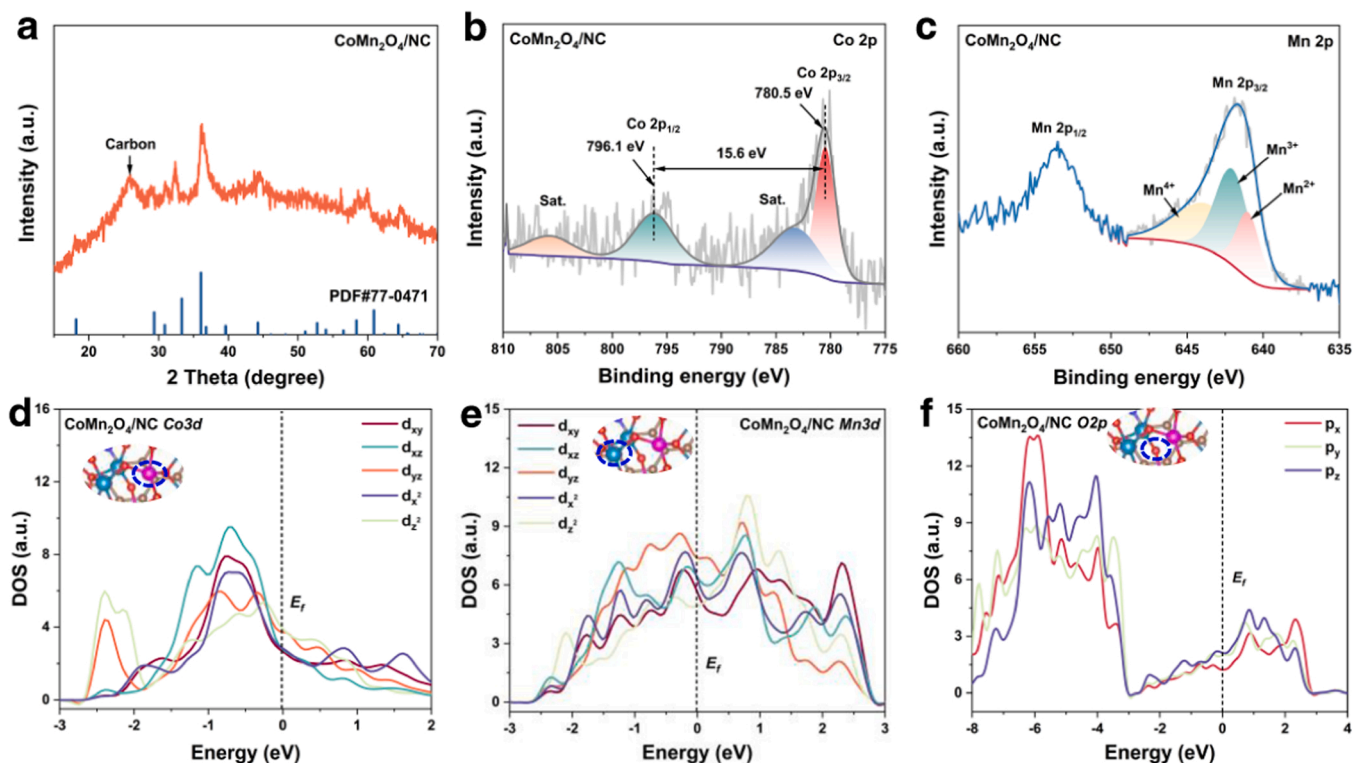
Fig. 2. (a) XRD pattern of $CoMn_2O_4/NC$. High-resolution XPS spectra of (b) Co 2p and (c) Mn 2p regions of $CoMn_2O_4/NC$. DOS of (d) Co 3d, (e) Mn 3d and (f) O 2p for $CoMn_2O_4/NC$.
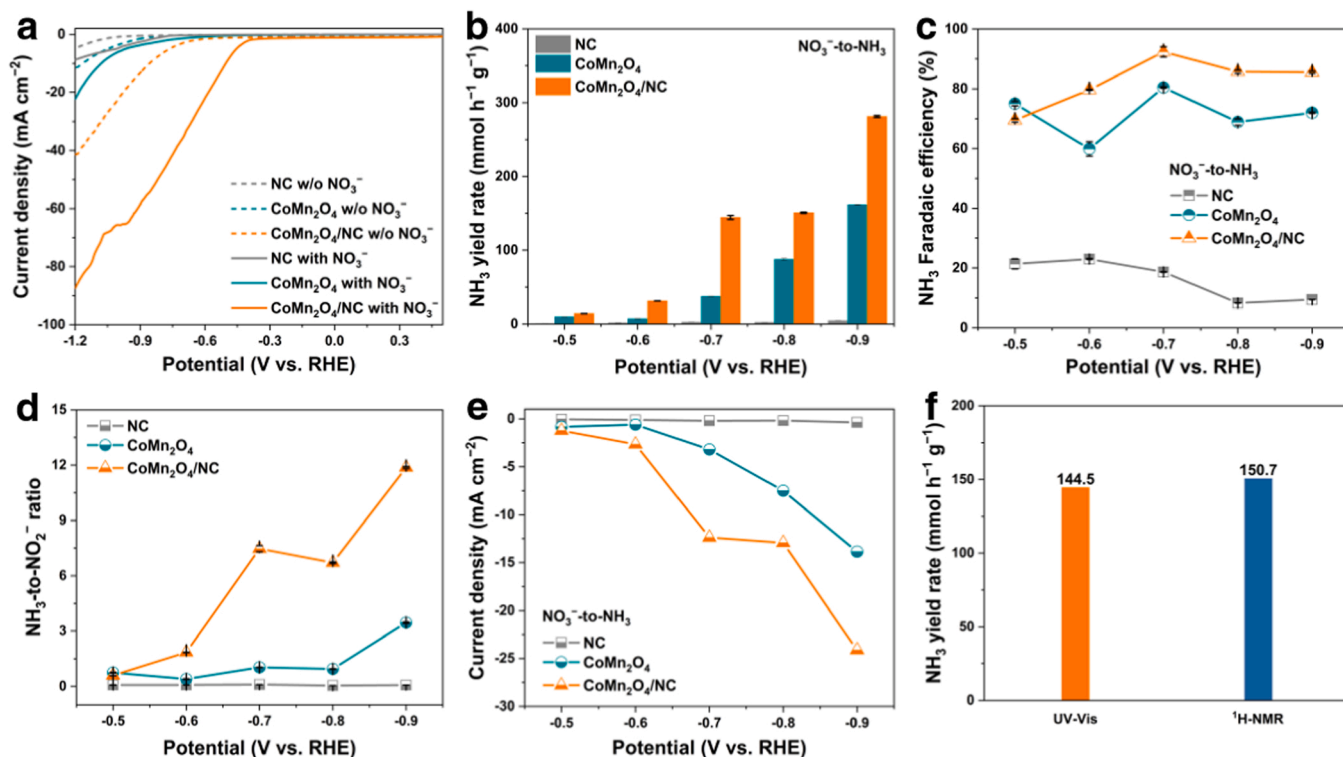

Fig. 3. (a) LSV curves of $CoMn_2O_4/NC$, $CoMn_2O_4$ and NC in 0.1 M Na_2SO_4 with and without 0.1 M NO_3^-. The NH_3 (b) yield rate and (c) Faradaic efficiency of NO_3^-RR for $CoMn_2O_4/NC$, $CoMn_2O_4$ and NC at different potentials. (d) The NH_3-to-NO_2^- product ratios for different catalysts. (e) The partial current densities of NH_3 evolution for different catalysts with 0.1 M NO_3^-. (f) The NH_3 yield rate of $CoMn_2O_4/NC$ detected by UV-Vis and ^1H NMR method at -0.7 V vs. RHE.

investigated at the potential range from -0.5 to -0.9 V vs. RHE (Fig. S10a-c). The yield rate of NH_3 increases with decreasing potential, while the Faradaic efficiency shows a typical volcano-type trend (Fig. 3b and c). For $CoMn_2O_4/NC$, the NH_3 Faradaic efficiency reaches the maximum value of 92.4% at -0.7 V vs. RHE with a yield rate of 144.5 mmol h^{-1} g^{-1} (1040.1 μg h^{-1} cm^{-2}), which is higher than that of most transition metal-base catalysts previously reported (Fig. S11 and Table S2) [20,22,24,27,28,42–47]. In contrast, the optimal NH_3 Faradaic efficiency and yield rate of $CoMn_2O_4$ are 80.4% and 37.3 mmol h^{-1} g^{-1} (268.6 μg h^{-1} cm^{-2}) under the same conditions, respectively.

Nitrite (NO_2^-) is the main by-product of NO_3^-RR, and the yield rate and Faradaic efficiency of NO_2^- were also considered. By comparison, the activity of NO_3^--to-NO_2^- on $CoMn_2O_4$ and NC is higher than that of $CoMn_2O_4/NC$ (Fig. S12). The NO_2^- yield rate and Faradaic efficiency of $CoMn_2O_4/NC$ are 16.8 mmol h^{-1} g^{-1} (308.2 μg h^{-1} cm^{-2}) and 2.7% at -0.7 V vs. RHE, respectively. Notably, NC exhibited more elevated NO_2^- Faraday efficiency, consistent with our previous report [27]. The N_2H_4 and H_2, as possible by-products of NO_3^-RR, were also investigated (Fig. S13). The results confirmed that no obvious N_2H_4 was detected, and only a trace amount of H_2 was detected at negative potentials (i.e., -0.8 and -0.9 V vs. RHE). Interestingly, the total Faradaic efficiency of NH_3 and NO_2^- reveals that $CoMn_2O_4/NC$ and $CoMn_2O_4$ could effectively suppress hydrogen evolution reaction (HER) (Fig. S14). As shown in Fig. 3d, the Faradaic efficiency ratio of NH_3-to-NO_2^- demonstrated that $CoMn_2O_4/NC$ always has more favorable NH_3 evolution than others. As expected, the NH_3 partial current density of $CoMn_2O_4/NC$ is still more negative than $CoMn_2O_4$ and NC at applied potentials (Fig. 3e). A series of control and isotope labeling (i.e., $^{15}NO_3^-$) experiments confirmed that

the NH_3 detected in this system originated from the electrochemical reduction of nitrate species (Fig. S15 and 16). Additionally, the NH_3 yield analyzed by ^1H NMR (150.7 mmol h^{-1} g^{-1}, 1085.1 μg h^{-1} cm^{-2}) is consistent with the Ultraviolet visible (UV–vis, i.e., indophenol blue) test results, which verifies the accuracy of the detection method (Fig. 3f). Both yield rate and Faradaic efficiency of NH_3 are well maintained after consecutive cycles, implying good stability of $CoMn_2O_4/NC$ (Fig. S17).

As previously noted, the NO_2^- is an inevitable intermediate species for electrochemical NO_3^-RR production of NH_3 [14,22]. Therefore, the activity of the catalyst to NO_2^- is one of the crucial evaluation indicators. As shown in Fig. 4a, the current density of NO_2^-RR over all catalysts delivers a similar trend to that of NO_3^-RR, with a more negative current density and more positive onset potential. The performance of NO_2^-RR was evaluated at the potential range of $-0.5 \sim -0.9$ V vs. RHE (Fig. S10d-f). The yield rate of NH_3 gradually increased with decreasing potential, similar to NO_3^-RR, while $CoMn_2O_4$ was superior to $CoMn_2O_4/NC$ at the same potential (Fig. 4b). It is worth noting that $CoMn_2O_4/NC$ has better NH_3 Faradaic efficiency, reaching more than 95% at $-0.6 \sim -0.9$ V vs. RHE (Fig. 4c), which is obtained the maximum of 100% at -0.7 V vs. RHE, with a yield rate and NH_3 partial current density of 180 mmol h^{-1} g^{-1} (1295.9 μg h^{-1} cm^{-2}) and -11.6 mA cm^{-2} (Fig. 4b and d), respectively. For $CoMn_2O_4$, NH_3 Faradaic efficiency decreases significantly when the applied potential is lower than -0.7 V vs. RHE (96.2%). The above results indicate that although $CoMn_2O_4$ has a better activity for NO_2^-RR, the presence of carbon species can significantly improve the adsorption of $^*NO_3$.

Electrochemical in situ Raman spectroscopy was employed to monitor possible changes in the catalyst surface structure and
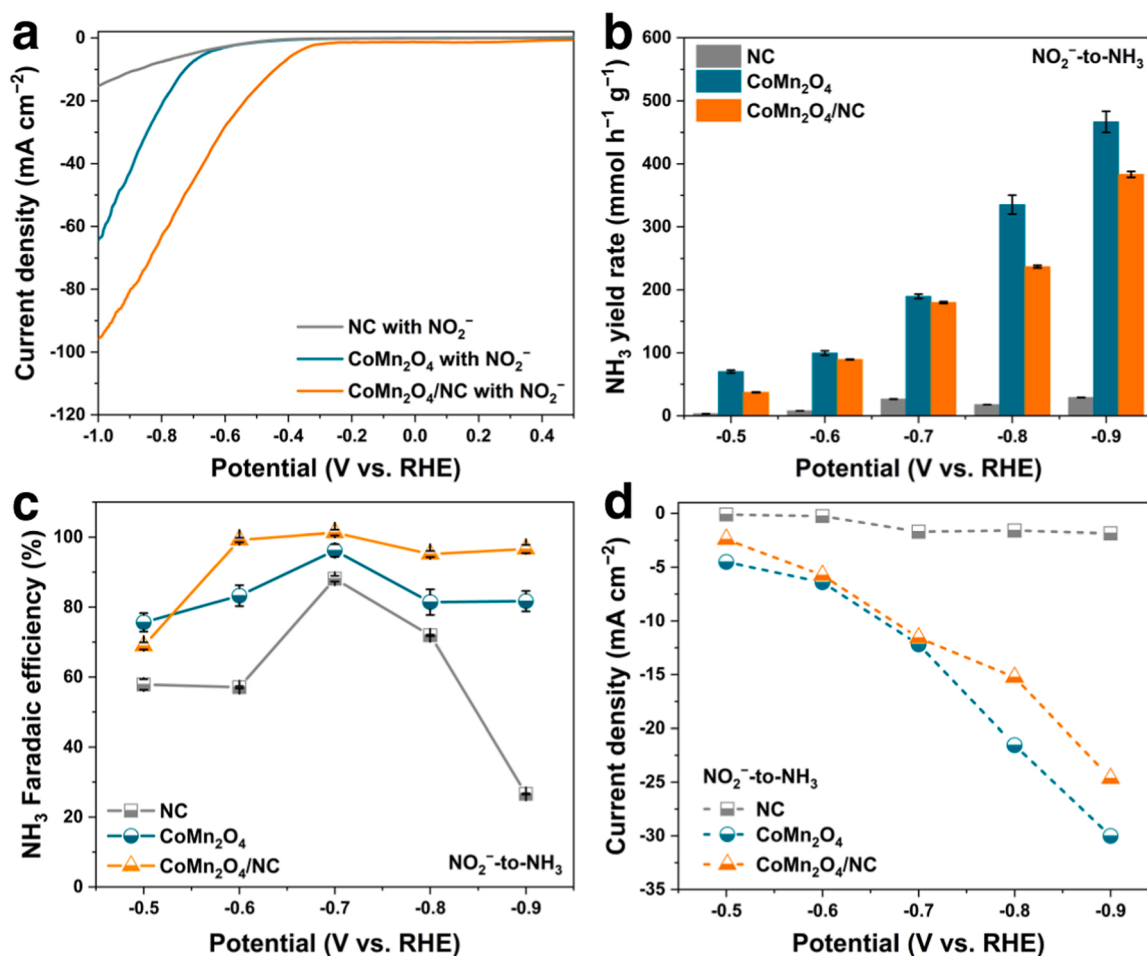
Fig. 4. (a) LSV curves of $CoMn_2O_4$, $CoMn_2O_4/NC$ and NC in 0.1 M Na_2SO_4 with 0.1 M NO_2^-. The NH_3 (b) yield rate and (c) Faradaic efficiency of NO_2^-RR for $CoMn_2O_4/NC$, $CoMn_2O_4$ and NC at different potentials. (d) The partial current densities of NH_3 evolution for different catalysts with 0.1 M NO_2^-.

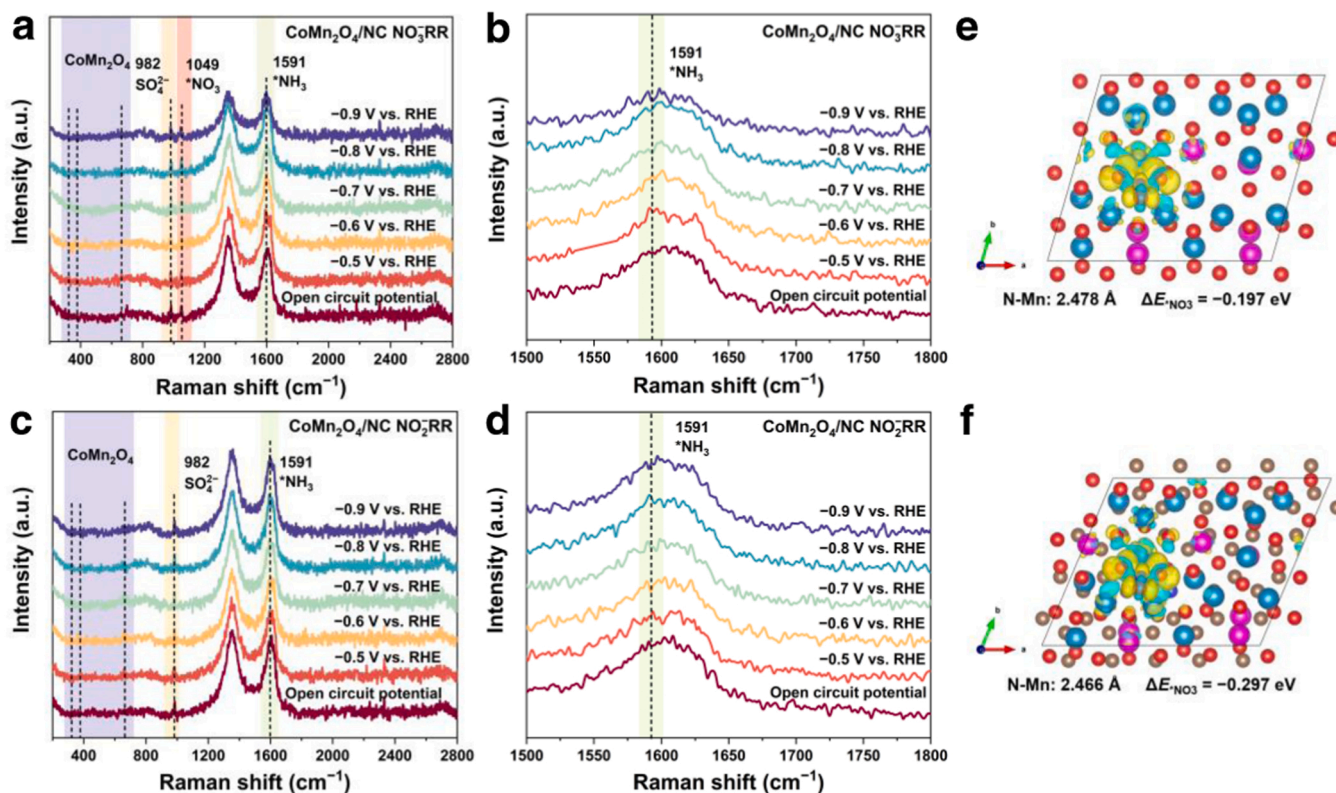**Fig. 5.** Electrochemical in situ Raman spectra of CoMn$_2$O$_4$/NC for (a and b) NO$_3^-$RR and (c and d) NO$_2^-$RR. Charge density difference of *NO$_3$ configuration at (e) CoMn$_2$O$_4$/NC and (f) CoMn$_2$O$_4$ (Cyan and yellow regions represent negative and positive charges, respectively, with iso-surfaces energy density of 0.002 e Å^{-3}).

intermediate species during the reaction (Figs. 5 and S18). For CoMn$_2$O$_4$/NC, the two peaks at 1347 and 1600 cm^{-1} belong to the D and G bands of carbon species [48], respectively, whereas they do not appear in CoMn$_2$O$_4$ (Fig. S18), which is consistent with the XRD and XPS results. The peaks at 323, 378 and 664 cm^{-1} were assigned to CoMn$_2$O$_4$ and did not change significantly during the reaction [49], indicating good structural stability. Besides, the Raman peak at 982 and 1049 cm^{-1} was referenced as adsorbed sulfate species (SO$_4^{2-}$) and NO$_3^-$ on the surface of catalysts [50,51], respectively. It is worth noting that a new peak appears around 1591 cm^{-1}, which is assigned to *NH$_3$ [51,52]. To investigate the adsorption behavior of NO$_3^-$ on the catalyst surface, the charge density difference of *NO$_3$ on CoMn$_2$O$_4$/NC and CoMn$_2$O$_4$ was plotted. As shown in Fig. 5e and f, a stronger charge transfer tendency existed between *NO$_3$ and CoMn$_2$O$_4$/NC, which endow a larger free adsorption energy (0.297 eV) and a shorter N-Mn bond length (2.466 Å), indicating a stronger adsorption ability of *NO$_3$ on CoMn$_2$O$_4$/NC. The strong adsorption capacity of NO$_3^-$ on CoMn$_2$O$_4$/NC can inhibit the competitive adsorption of other anions and ensure the subsequent hydrogenation process.
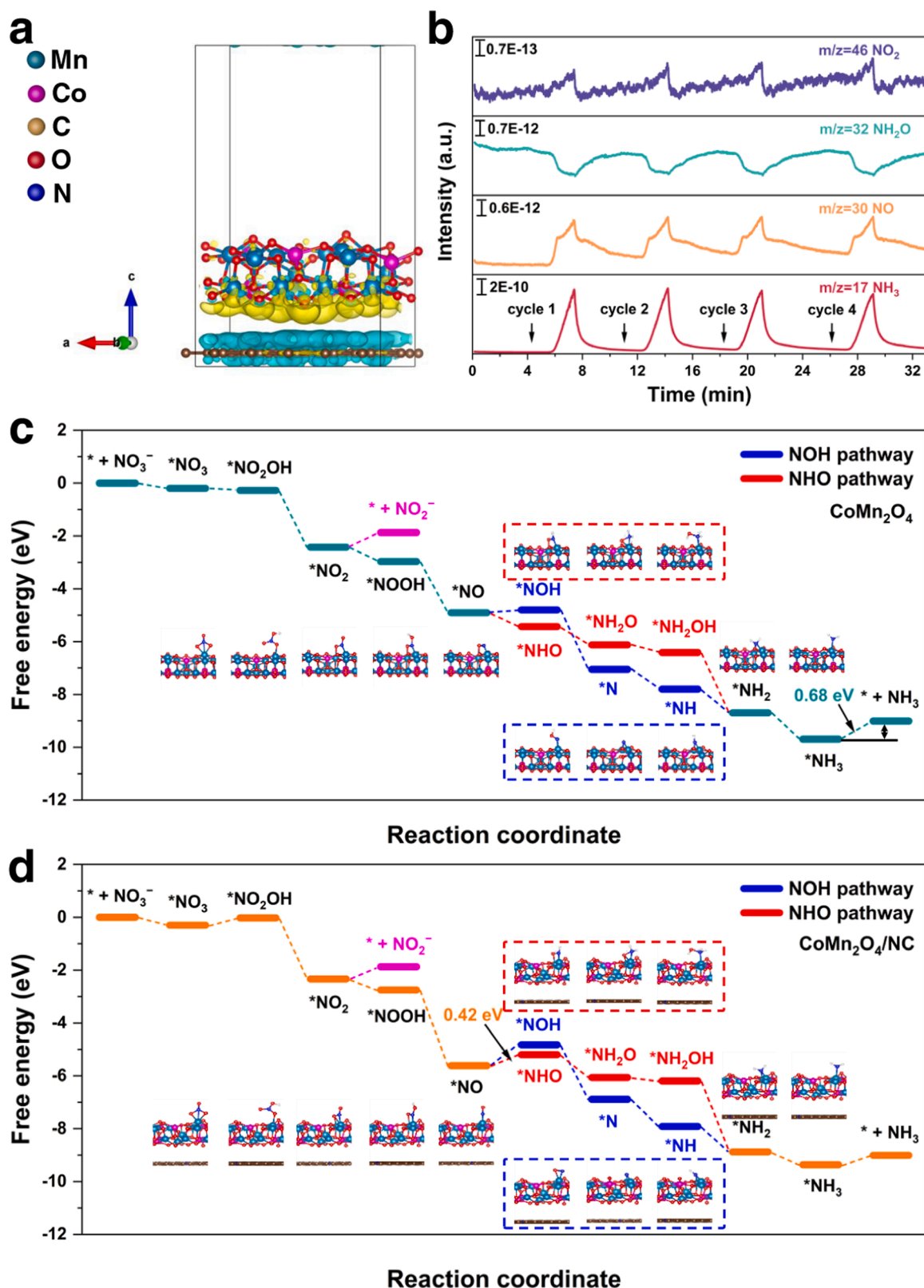
Charge density difference results of CoMn$_2$O$_4$/NC demonstrate that carbon species induce CoMn$_2$O$_4$ electron delocalization to form more positively charged regions (Fig. 6a), consistent with the DOS results. In addition, intermediates and products that perhaps present during the reaction were detected by online in situ differential electrochemical mass spectrometry (DEMS). As shown in Fig. 6b, four strongly mass-to-charge ratios (*m/z*) signals, i.e., 17, 30, 32 and 46, were detected in four LSV cycles, belonging to NH$_3$, NO, NH$_2$O and NO$_2$, respectively. To further illustrate the underlying reaction pathways existing on the catalyst surface and the adsorption behavior of each intermediate species, we obtained the free-energy diagrams using Density functional theory (DFT) calculations. The optimal adsorption model of each intermediate on the catalyst surface is shown in Figs. S19 and S20. Typically, the potential pathways of *NO$_3$-to-*NH$_3$ can be divided into *NOH

and *NHO [53]. Fig. 6c, d reveal the free energy diagrams for NO$_3^-$RR on CoMn$_2$O$_4$ and CoMn$_2$O$_4$/NC (U = 0 V and pH = 7). The higher ΔG for the desorption of *NO$_2$ on CoMn$_2$O$_4$ (0.554 eV) and CoMn$_2$O$_4$/NC (0.465 eV) will inhibit the formation the by-product of NO$_2^-$, consistent with the DEMS results. The *NHO pathway thermodynamics is more favorable because a lower ΔG of *NO-to-*NHO (vs. *NO-to-*NOH) on CoMn$_2$O$_4$ (−0.52 vs. 0.11 eV) and CoMn$_2$O$_4$/NC (0.42 vs. 0.79 eV). On the CoMn$_2$O$_4$ surface, the desorption of *NH$_3$ is the potential rate-determining step (RDS) with the highest ΔG of 0.68 eV, which is higher than CoMn$_2$O$_4$/NC (*NO-to-*NHO). More importantly, the adsorption free energy of *H on the surface of CoMn$_2$O$_4$/NC is − 0.368 eV, which is more negative than CoMn$_2$O$_4$ (−0.129 eV) (Fig. S21). This result confirms that the presence of carbon species can effectively inhibit the HER activity of CoMn$_2$O$_4$, thus endowing CoMn$_2$O$_4$/NC with efficient electrochemical NO$_3^-$ conversion into NH$_3$, consistent with the experimental results, especially at more negative potentials. Therefore, the carbon species not only boost NO$_3^-$RR of CoMn$_2$O$_4$ by decreasing the ΔG of RDS, but also inhibit the HER by enhancing the *H adsorption capacity.

3.3. Electrocatalytic performance for NO$_2^-$RR||BOR

The oxygen evolution reaction (OER) is an unavoidable anodic half-reaction for conventional electrochemical NO$_3^-$RR. However, sluggish kinetics of OER, with standard electrode potential (E$^\theta$) of 1.23 V vs. RHE, is much higher than that of alcohol oxidation reaction (AOR) [54, 55]. For example, the E$^\theta$ for benzyl alcohol oxidation reaction (BOR) is only 0.48 V vs. RHE [56], which is a perfect alternative to supersede OER. The coupled AOR not only reduce the overpotential of the system by increasing the onset potential, but also obtain high-value-added anodic oxidation products, such as organic acids, aldehydes and ketones. Inspired by this, we constructed a two-electrode electrolyzer by coupling NO$_2^-$RR and BOR with CoMn$_2$O$_4$/NC loaded carbon cloth and

Fig. 6. (a) Charge density difference of CoMn$_2$O$_4$/NC. (Cyan and yellow regions represent negative and positive charges, respectively, with iso-surfaces energy density of 0.0004 e Å^{-3}.) (b) In situ DEMS measurements of CoMn$_2$O$_4$/NC for NO$_3^-$RR. Free energy diagram (U = 0 V and pH = 7) for NO$_3^-$RR on the substrate of (c) CoMn$_2$O$_4$ and (d) CoMn$_2$O$_4$/NC.
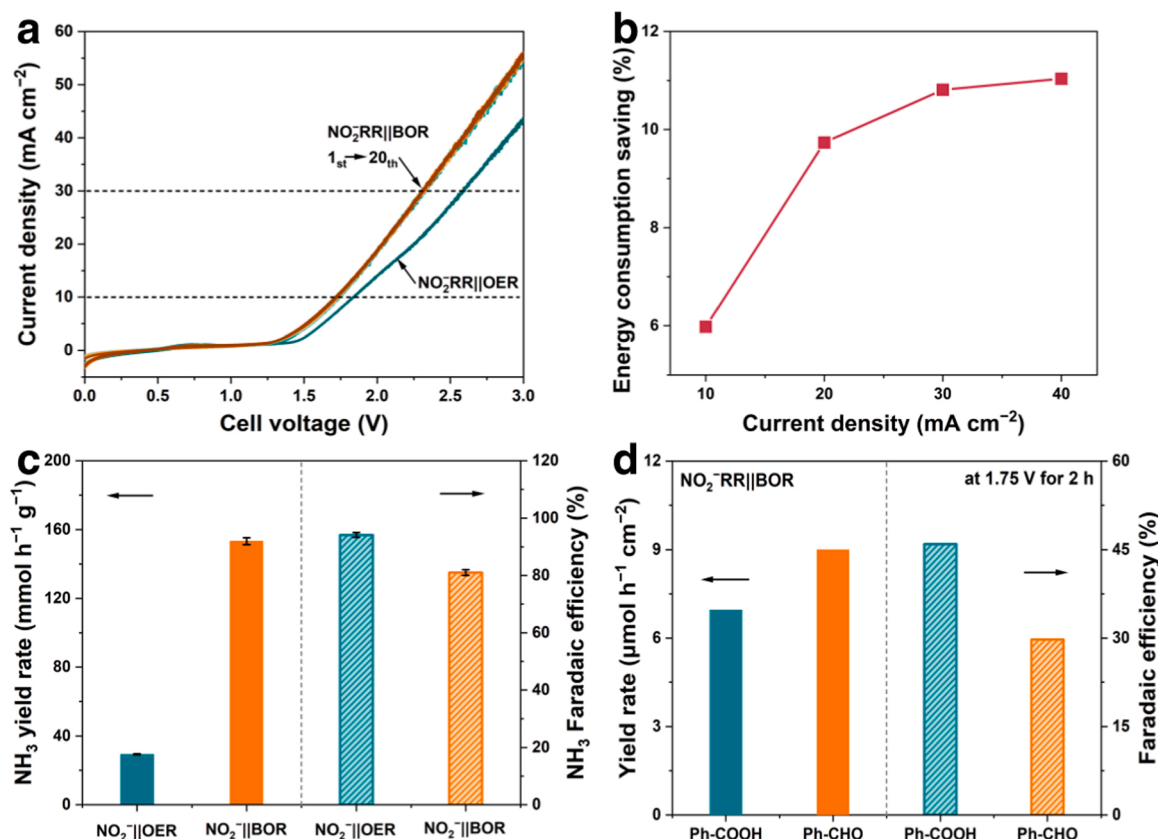
Fig. 7. (a) LSV curves of NO_2^-RR coupling OER and BOR in two-electrode system. (b) The energy consumption savings of $NO_2^-RR||BOR$ at different current densities. (c) NH_3 yield rate and Faradaic efficiency at 1.75 V for 2 h in two-electrode system. (d) The anode corresponding products yield rate and Faradaic efficiency of $NO_2^-RR||BOR$.

nickel foam as cathode and anode working electrodes. As shown in Fig. 7a, $NO_2^-RR||BOR$ has a lower voltage at the same current density as $NO_2^-RR||OER$. Moreover, 20th consecutive LSV results confirm that the electrode material has good stability. Notably, the energy consumption savings of the coupled system increases with increasing current density (Fig. 7b). After 2 h of electrolysis, the cathodic NH_3 yield rate for $NO_2^-RR||BOR$ is 153.3 mmol h^{-1} g^{-1} (1493.6 µg h^{-1} cm^{-2}), which is 5.2 times that of $NO_2^-RR||OER$ (29.4 mmol h^{-1} g^{-1}, 422.7 µg h^{-1} cm^{-2}) (Fig. 7c and S22a). Notably, the NH_3 Faradaic efficiency of $NO_2^-RR||BOR$ (81%) is slightly lower than that of $NO_2^-RR||OER$ (94.1%), probably due to the promotion of cathodic HER by coupled BOR. The anode benzoic acid (Ph-COOH) and benzaldehyde yield (Ph-COH) rate were 7 and 9 µmol h^{-1} cm^{-2}, respectively, and the Faradaic efficiencies were 46% and 29.7% (Fig. 7d). The long-term electrolysis (24 h) of $NO_2^-RR||BOR$ experiments further confirmed the excellent stability of the system (Fig. S22b). In addition, the XRD, SEM and XPS characterization results of the electrode materials after the long-term reaction confirmed that $CoMn_2O_4/NC$ has good durability (Fig. S23). The above results indicate that coupling and BOR and NO_2^-RR is feasible, not only energy-effectively but also generating high-value-added anode products.

4. Conclusion

We successfully prepared $CoMn_2O_4/NC$ via facile electrospinning and pyrolysis method. The composite displayed a multichannel fibers structure with highly dispersed $CoMn_2O_4$ uniformly anchored. The $CoMn_2O_4/NC$ exhibits an excellent electrocatalytic performance toward the NO_3^-RR at ambient conditions. The maximum NH_3 Faradaic efficiency of 92.4% at − 0.7 V vs. RHE, with a yield rate of 144.5 mmol h^{-1} g^{-1} (1040.1 µg h^{-1} cm^{-2}). Electrochemical in situ Raman spectra

indicated that the structure of the catalyst had excellent stability during the NO_3^-RR process. The DFT calculation results demonstrated that the existence of carbon species induced the electron delocalization of $CoMn_2O_4$, which significantly promoted NO_3^-RR by reducing the ΔG of RDS (*NO-to-*NHO, 0.42 eV). A full-cell electrolyzer is constructed by coupling BOR and NO_2^-RR to realize NH_3 synthesis at low voltage and obtain high value-added products at the anode simultaneously. This work provides a reference for energy-effective and environmentally friendly strategy to electrochemical NH_3 synthesis.

CRediT authorship contribution statement

Zhaodong Niu: Investigation, Data curation, Methodology, Software, Visualization, Writing – original draft, Visualization, **Shiying Fan:** Methodology, Software, Visualization, Writing – review & editing, Resources, **Xinyong Li:** Conceptualization, Formal analysis, Resources, Writing – review & editing, Supervision, **Juan Duan:** Methodology, Software, Visualization, Writing – review & editing, **Aicheng Chen:** Supervision, Conceptualization, Writing – review & editing.

Declaration of Competing Interest

The authors declare that they have no known competing financial interests or personal relationships that could have appeared to influence the work reported in this paper.

Data availability

The data that has been used is confidential.

Acknowledgments

Appendix A. Supplementary material

Supplementary data associated with this article can be found in the online version at doi:10.1016/j.apcatb.2022.122090.

References

[1] S.L. Foster, S.I.P. Bakovic, R.D. Duda, S. Maheshwari, R.D. Milton, S.D. Minteer, M. J. Janik, J.N. Renner, L.F. Greenlee, Catalysts for nitrogen reduction to ammonia, Nat. Catal. 1 (2018) 490–500.

[2] J.H. Montoya, C. Tsai, A. Vojvodic, J.K. Norskov, The challenge of electrochemical ammonia synthesis: a new perspective on the role of nitrogen scaling relations, ChemSusChem 8 (2015) 2180–2186.

[3] J. Sun, D. Alam, R. Daiyan, H. Masood, T. Zhang, R. Zhou, P.J. Cullen, E.C. Lovell, A. Jalili, R. Amal, A hybrid plasma electrocatalytic process for sustainable ammonia production, Energy Environ. Sci. 14 (2021) 865–872.

[4] M. Qin, X. Li, G. Gan, L. Wang, S. Fan, Z. Yin, G. Chen, Boosting electrocatalytic nitrogen fixation with co-n3 site-decorated porous carbon, ACS Sustain. Chem. Eng. 8 (2020) 13430–13439.

[5] D. Chen, S. Zhang, X. Bu, R. Zhang, Q. Quan, Z. Lai, W. Wang, Y. Meng, D. Yin, S. Yip, C. Liu, C. Zhi, J.C. Ho, Synergistic modulation of local environment for electrochemical nitrate reduction via asymmetric vacancies and adjacent ion clusters, Nano Energy 98 (2022), 107338.

[6] Y. Huang, J. Long, Y. Wang, N. Meng, Y. Yu, S. Lu, J. Xiao, B. Zhang, Engineering nitrogen vacancy in polymeric carbon nitride for nitrate electroreduction to ammonia, ACS Appl. Mater. Interfaces 13 (2021) 54967–54973.

[7] C. Lv, L. Zhong, H. Liu, Z. Fang, C. Yan, M. Chen, Y. Kong, C. Lee, D. Liu, S. Li, J. Liu, L. Song, G. Chen, Q. Yan, G. Yu, Selective electrocatalytic synthesis of urea with nitrate and carbon dioxide, Nat. Sustain. 4 (2021) 868–876.

[8] H. Hirakawa, M. Hashimoto, Y. Shiraishi, T. Hirai, Selective nitrate-to-ammonia transformation on surface defects of titanium dioxide photocatalysts, ACS Catal. 7 (2017) 3713–3720.

[9] S. Zhai, D.J. Jacob, X. Wang, Z. Liu, T. Wen, V. Shah, K. Li, J.M. Moch, K.H. Bates, S. Song, L. Shen, Y. Zhang, G. Luo, F. Yu, Y. Sun, L. Wang, M. Qi, J. Tao, K. Gui, H. Xu, Q. Zhang, T. Zhao, Y. Wang, H.C. Lee, H. Choi, H. Liao, Control of particulate nitrate air pollution in China, Nat. Geosci. 14 (2021) 389–395.

[10] L. Wei, D.-J. Liu, B.A. Rosales, J.W. Evans, J. Vela, Mild and selective hydrogenation of nitrate to ammonia in the absence of noble metals, ACS Catal. 10 (2020) 3618–3628.

[11] L. Li, C. Tang, X. Cui, Y. Zheng, X. Wang, H. Xu, S. Zhang, T. Shao, K. Davey, S. Z. Qiao, Efficient nitrogen fixation to ammonia through integration of plasma oxidation with electrocatalytic reduction, Angew. Chem. Int. Ed. 60 (2021) 14131–14137.

[12] D.R. MacFarlane, P.V. Cherepanov, J. Choi, B.H.R. Suryanto, R.Y. Hodgetts, J. M. Bakker, F.M. Ferrero Vallana, A.N. Simonov, A roadmap to the ammonia economy, Joule 4 (2020) 1186–1205.

[13] P.H. van Langevelde, I. Katsounaros, M.T.M. Koper, Electrocatalytic nitrate reduction for sustainable ammonia production, Joule 5 (2021) 290–294.

[14] Y. Wang, C. Wang, M. Li, Y. Yu, B. Zhang, Nitrate electroreduction: mechanism insight, in situ characterization, performance evaluation, and challenges, Chem. Soc. Rev. 50 (2021) 6720–6733.

[15] J. Lim, C.-Y. Liu, J. Park, Y.-H. Liu, T.P. Senftle, S.W. Lee, M.C. Hatzell, Structure sensitivity of Pd facets for enhanced electrochemical nitrate reduction to ammonia, ACS Catal. 11 (2021) 7568–7577.

[16] J. Li, G. Zhan, J. Yang, F. Quan, C. Mao, Y. Liu, B. Wang, F. Lei, L. Li, A.W.M. Chan, L. Xu, Y. Shi, Y. Du, W. Hao, P.K. Wong, J. Wang, S.X. Dou, L. Zhang, J.C. Yu, Efficient ammonia electrosynthesis from nitrate on strained ruthenium nanoclusters, J. Am. Chem. Soc. 142 (2020) 7036–7046.

[17] H. Liu, J. Park, Y. Chen, Y. Qiu, Y. Cheng, K. Srivastava, S. Gu, B.H. Shanks, L. T. Roling, W. Li, Electrocatalytic nitrate reduction on oxide-derived silver with tunable selectivity to nitrite and ammonia, ACS Catal. 11 (2021) 8431–8442.

[18] R. Jia, Y. Wang, C. Wang, Y. Ling, Y. Yu, B. Zhang, Boosting selective nitrate electroreduction to ammonium by constructing oxygen vacancies in TiO2, ACS Catal. 10 (2020) 3533–3540.

[19] X. Deng, Y. Yang, L. Wang, X.Z. Fu, J.L. Luo, Metallic Co nanoarray catalyzes selective NH3 production from electrochemical nitrate reduction at current densities exceeding 2 A cm^{-2}, Adv. Sci. 8 (2021) 2004390.

[20] Z. Niu, S. Fan, X. Li, P. Wang, M.O. Tadé, S. Liu, Optimizing oxidation state of octahedral copper for boosting electroreduction nitrate to ammonia, ACS Appl. Energy Mater. 5 (2022) 3339–3345.

[21] H. Wang, Q. Mao, T. Ren, T. Zhou, K. Deng, Z. Wang, X. Li, Y. Xu, L. Wang, Synergism of interfaces and defects: Cu/oxygen vacancy-rich Cu-Mn3O4 heterostructured ultrathin nanosheet arrays for selective nitrate electroreduction to ammonia, ACS Appl. Mater. Interfaces 13 (2021) 44733–44741.

[22] Z. Niu, S. Fan, X. Li, Z. Liu, J. Wang, J. Duan, M.O. Tade, S. Liu, Facile tailoring of the electronic structure and the d-band center of copper-doped cobaltate for efficient nitrate electrochemical hydrogenation, ACS Appl. Mater. Interfaces 14 (2022) 35477–35484.

[23] J. Li, D. Zhao, L. Zhang, Y. Ren, L. Yue, Z. Li, S. Sun, Y. Luo, Q. Chen, T. Li, K. Dong, Q. Liu, Q. Kong, X. Sun, Boosting electrochemical nitrate-to-ammonia conversion by self-supported MnCo2O4 nanowire array, J. Colloid Interface Sci. 629 (2022) 805–812.

[24] Z. Li, J. Liang, Q. Liu, L. Xie, L. Zhang, Y. Ren, L. Yue, N. Li, B. Tang, A.A. Alshehri, M.S. Hamdy, Y. Luo, Q. Kong, X. Sun, High-efficiency ammonia electrosynthesis via selective reduction of nitrate on ZnCo2O4 nanosheet array, Mater. Today Phys. 23 (2022), 100619.

[25] Z. Deng, J. Liang, Q. Liu, C. Ma, L. Xie, L. Yue, Y. Ren, T. Li, Y. Luo, N. Li, B. Tang, A. Ali Alshehri, I. Shakir, P.O. Agboola, S. Yan, B. Zheng, J. Du, Q. Kong, X. Sun, High-efficiency ammonia electrosynthesis on self-supported Co2AlO4 nanoarray in neutral media by selective reduction of nitrate, Chem. Eng. J. 435 (2022), 135104.

[26] G.-F. Chen, Y. Yuan, H. Jiang, S.-Y. Ren, L.-X. Ding, L. Ma, T. Wu, J. Lu, H. Wang, Electrochemical reduction of nitrate to ammonia via direct eight-electron transfer using a copper-molecular solid catalyst, Nat. Energy 5 (2020) 605–613.

[27] Z. Niu, S. Fan, X. Li, P. Wang, Z. Liu, J. Wang, C. Bai, D. Zhang, Bifunctional copper-cobalt spinel electrocatalysts for efficient tandem-like nitrate reduction to ammonia, Chem. Eng. J. 450 (2022), 138343.

[28] W.J. Sun, H.Q. Ji, L.X. Li, H.Y. Zhang, Z.K. Wang, J.H. He, J.M. Lu, Built-in electric field triggered interfacial accumulation effect for efficient nitrate removal at ultra-low concentration and electroreduction to ammonia, Angew. Chem. Int. Ed. Engl. 60 (2021) 22933–22939.

[29] W. He, J. Zhang, S. Dieckhofer, S. Varhade, A.C. Brix, A. Lielpetere, S. Seisel, J.R. C. Junqueira, W. Schuhmann, Splicing the active phases of copper/cobalt-based catalysts achieves high-rate tandem electroreduction of nitrate to ammonia, Nat. Commun. 13 (2022) 1129.

[30] M. Qin, S. Fan, X. Li, Z. Niu, C. Bai, G. Chen, Highly efficient electrocatalytic upgrade of n-valeraldehyde to octane over Au SACs-NiMn2O4 spinel synergetic composites, Small 18 (2022), 2201359.

[31] Z. Song, Y. Liu, Y. Zhong, Q. Guo, J. Zeng, Z. Geng, Efficient electroreduction of nitrate into ammonia at ultralow concentrations via an enrichment effect, Adv. Mater. 34 (2022), e2204306.

[32] D.K. Yesudoss, H. Chun, B. Han, S. Shanmugam, Accelerated N2 reduction kinetics in hybrid interfaces of NbTiO4 and nitrogen-doped carbon nanorod via synergistic electronic coupling effect, Appl. Catal. B 304 (2022), 120938.

[33] S. Liu, X.F. Lu, J. Xiao, X. Wang, X.W.D. Lou, Bi2O3 nanosheets grown on multi-channel carbon matrix to catalyze efficient CO2 electroreduction to HCOOH, Angew. Chem. Int. Ed. 58 (2019) 13828–13833.

[34] J. Hafner, Ab-initio simulations of materials using VASP: density-functional theory and beyond, Comput. Chem. 29 (2008) 2044–2078.

[35] G.K. A, J.F. b, Efficiency of ab-initio total energy calculations for metals and semiconductors using a plane-wave basis set, Comput. Mater. Sci. 6 (1996) 15–50.

[36] P.E. Blochl, Projector augmented-wave method, J. Phys. Rev. B 50 (1994) 17953–17979.

[37] John P. Perdew, Matthias Ernzerhof, Kieron Burke, Erratum: Generalized gradient approximation made simple, Phys. Rev. Lett. 77 (1996) 3865–3868.

[38] C. Dong, C. Qu, Y. Qin, Q. Fu, H. Sun, X. Duan, Revealing the highly catalytic performance of spinel CoMn2O4 for toluene oxidation: involvement and replenishment of oxygen species using in situ designed-TP techniques, ACS Catal. 9 (2019) 6698–6710.

[39] G. Gan, X. Li, L. Wang, S. Fan, J. Li, F. Liang, A. Chen, Identification of catalytic active sites in nitrogen-doped carbon for electrocatalytic dechlorination of 1,2-dichloroethane, ACS Catal. 9 (2019) 10931–10939.

[40] A. Li, S. Kong, C. Guo, H. Ooka, K. Adachi, D. Hashizume, Q. Jiang, H. Han, J. Xiao, R. Nakamura, Enhancing the stability of cobalt spinel oxide towards sustainable oxygen evolution in acid, Nat. Catal. 5 (2022) 109–118.

[41] Y. Qin, S. Fan, X. Li, G. Gan, L. Wang, Z. Yin, X. Guo, M.O. Tadé, S. Liu, Peanut-shaped Cu—Mn nano-hollow spinel with oxygen vacancies as catalysts for low-temperature NO reduction by CO, ACS Appl. Nano Mater. 4 (2021) 11969–11979.

[42] Y. Wang, W. Zhou, R. Jia, Y. Yu, B. Zhang, Unveiling the activity origin of a copper-based electrocatalyst for selective nitrate reduction to ammonia, Angew. Chem. Int. Ed. 59 (2020) 5350–5354.

[43] J. Qin, L. Chen, K. Wu, X. Wang, Q. Zhao, L. Li, B. Liu, Z. Ye, Electrochemical synthesis of ammonium from nitrates via surface engineering in Cu2O(100) facets, ACS Appl. Energy Mater. 5 (2021) 71–76.

[44] C. Wang, Z. Liu, T. Hu, J. Li, L. Dong, F. Du, C. Li, C. Guo, Metasequoia-like nanocrystal of iron-doped copper for efficient electrocatalytic nitrate reduction into ammonia in neutral media, ChemSusChem 14 (2021) 1825–1829.

[45] L. Xie, L. Hu, Q. Liu, S. Sun, L. Zhang, D. Zhao, Q. Liu, J. Chen, J. Li, L. Ouyang, A. A. Alshehri, Q. Kong, X. Sun, High-performance electrochemical nitrate reduction to ammonia under ambient conditions using NiFe2O4 nanosheet arrays, Inorg. Chem. Front. 9 (2022) 3392–3397.

[46] P. Wei, J. Liang, Q. Liu, L. Xie, X. Tong, Y. Ren, T. Li, Y. Luo, N. Li, B. Tang, A. M. Asiri, M.S. Hamdy, Q. Kong, Z. Wang, X. Sun, Iron-doped cobalt oxide nanoarray for efficient electrocatalytic nitrate-to-ammonia conversion, J. Colloid Interface Sci. 615 (2022) 636–642.

[47] D. Zhao, J. Liang, J. Li, L. Zhang, K. Dong, L. Yue, Y. Luo, Y. Ren, Q. Liu, M. S. Hamdy, Q. Li, Q. Kong, X. Sun, A TiO$_{2-x}$ nanobelt array with oxygen vacancies:

an efficient electrocatalyst toward nitrite conversion to ammonia, Chem. Commun. 58 (2022) 3669–3672.

[48] G. Gan, X. Li, L. Wang, S. Fan, J. Mu, P. Wang, G. Chen, Active sites in single-atom Fe-N_x-C nanosheets for selective electrochemical dechlorination of 1,2-dichloro-ethane to ethylene, ACS Nano 14 (2020) 9929–9937.

[49] B. Poojitha, A. Shaji, S. Badola, S. Saha, Spin-phonon coupling in ferrimagnet spinel $CoMn_2O_4$, J. Chem. Phys. 156 (2022), 184701.

[50] Y. Wen, Z. Zhuang, H. Zhu, J. Hao, K. Chu, F. Lai, W. Zong, C. Wang, P. Ma, W. Dong, S. Lu, T. Liu, M. Du, Isolation of metalloid boron atoms in intermetallic carbide boosts the catalytic selectivity for electrocatalytic N_2 fixation, Adv. Energy Mater. 11 (2021), 2102138.

[51] J. Yu, Y. Qin, X. Wang, H. Zheng, K. Gao, H. Yang, L. Xie, Q. Hu, C. He, Boosting electrochemical nitrate-ammonia conversion via organic ligands-tuned proton transfer, Nano Energy 14 (2022), 107705-1168.

[52] D.P. Butcher, A.A. Gewirth, Nitrate reduction pathways on Cu single crystal surfaces: effect of oxide and Cl^-, Nano Energy 29 (2016) 457–465.

[53] J. Wang, C. Cai, Y. Wang, X. Yang, D. Wu, Y. Zhu, M. Li, M. Gu, M. Shao, Electrocatalytic reduction of nitrate to ammonia on low-cost ultrathin CoO_x nanosheets, ACS Catal. 11 (2021) 15135–15140.

[54] K. Xiang, D. Wu, X. Deng, M. Li, S. Chen, P. Hao, X. Guo, J.L. Luo, X.Z. Fu, Boosting H_2 generation coupled with selective oxidation of methanol into value-added chemical over cobalt hydroxide@hydroxysulfide nanosheets electrocatalysts, Adv. Funct. Mater. 30 (2020), 1909610.

[55] Y. Huang, R. Yang, G. Anandhababu, J. Xie, J. Lv, X. Zhao, X. Wang, M. Wu, Q. Li, Y. Wang, Cobalt/iron(oxides) heterostructures for efficient oxygen evolution and benzyl alcohol oxidation reactions, ACS Energy Lett. 3 (2018) 1854–1860.

[56] H. Huang, C. Yu, X. Han, H. Huang, Q. Wei, W. Guo, Z. Wang, J. Qiu, Ni, Co hydroxide triggers electrocatalytic production of high-purity benzoic acid over 400 mA cm^{-2}, Energy Environ. Sci. 13 (2020) 4990–4999.